Article

Fabrication of Mesoporous Silica Nanoparticle-Decorated Graphene Oxide Sheets for the Effective Removal of Lead (Pb^{2+}) from Water

Yana Bagbi* and Pratima R. Solanki*

Read Online

| ACCESS | Metrics & More | Article Recommendations | SI Supporting Information |

ABSTRACT: Mesoporous silica nanoparticle-decorated graphene oxide nanosheets (MSiO$_2$-GO) were synthesized and characterized for the active removal of lead (Pb^{2+}) from the water. MSiO$_2$ NPs were prepared via an ultrasonication method using tetraethyl orthosilicate (TEOS), and GO sheets were obtained via a modified Hummers' method. X-ray diffraction, UV−vis spectroscopy, Fourier transform infrared spectroscopy, and energy dispersive X-ray spectroscopy specified the composition of MSiO$_2$ NPs and GO sheets. The surface charge and texture of the MSiO$_2$-GO nanosheets were obtained using the ζ-potential technique and by field emission scanning electron microscopy. The relative cytotoxicity test of MSiO$_2$ NPs and MSiO$_2$-GO nanosheets was performed on Murine Raw 264.7 cells before implying the treatment of water. Adsorption of Pb^{2+} ions on MSiO$_2$-GO nanosheets was examined at various parameters such as different aqueous pH values (2.0–10.0), MSiO$_2$-GO nanosheet doses (3, 5, 10, 15, 20 mg L^{-1}), time intervals (2−30 min), and temperatures (25−45 °C). About 90% of Pb^{2+} ions were removed from water within 30 min (MSiO$_2$-GO dose: 15 mg L^{-1}; initial Pb^{2+} ions: 50 mg L^{-1}; temperature: 25 °C; shaking speed: 200 rpm). The maximal uptake of Pb^{2+} was obtained at solution pH 6.0. Pseudo-first- and pseudo-second-order kinetic rate equations describe the sorption dynamic data. Pb^{2+} sorption isotherms were modeled using the Freundlich and Langmuir isotherm models. The possible mechanism of binding of Pb^{2+} ions onto MSiO$_2$-GO nanosheets has been discussed. The exhausted MSiO$_2$-GO nanosheets were successfully regenerated using 0.005 M HNO$_3$ as the desorbing agent.
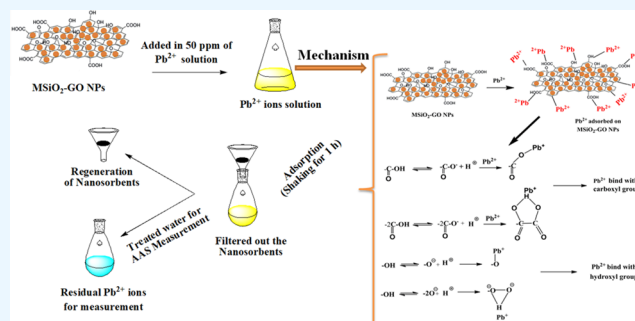
1. INTRODUCTION

Water pollution with heavy metals is a chronic problem plaguing almost all countries. The industrial and anthropogenic activities have made the situation worse. Since the heavy metals easily seep into water through the earth's surface, a reliable and economical solution to get rid of these contaminations from water is of utmost importance.[1−3] Moreover, these heavy metals, in the long run, are extremely hazardous for humans, plants, and animals.[2,3] Lead (Pb^{2+}) is one such heavy metal that is extremely toxic even in small amounts.[3,4] The contamination of the water by lead could be due to many activities such as discharging of untreated wastewater of battery and paint industries, through water supply pipes since metal pipes contain lead.[5−8] Out of the various methods available for the separation of heavy metals from water, the adsorption technique is most favored due to its economic viability and simplicity.[7−9]

Recently, the carbon-based material graphene oxide (GO) has been making ripples in the research arena due to the various outstanding properties it holds that could pave the way to numerous applications.[10,11] One of the potential applications of GO which has recently been explored is as a new sorbent for the purification of water, due to its excellent properties such as large surface area, high mobility of charge carriers, low cost, eco-friendliness, and thermal and chemical stability.[11,12] Also,

hexagonal arrays of carbon atoms provide strong fundamental interactions with other molecules.[4] Furthermore, engineered GO nanosheets contain several functional groups such as hydroxyl (−OH), carboxyl (−COOH), and epoxy groups (−C═O).[12,13] These functional groups increase the dispensability of GO and enhance the excellent adsorption sites for various contaminants, including metal ions in water.

However, GO layers have a significant demerit of aggregations, which leads to the folding of graphene sheets, thereby reducing its specific surface area, mechanical strength, and structural properties, hence reducing adsorption capacities.[12,13] Therefore, the incorporation of metal/metal oxide/nonmetallic oxide nanoparticles in the GO nanosheets or modification of GO with specific functional groups may decrease the aggregation and increase its mechanical strength and hence the active surface area.[9,13]
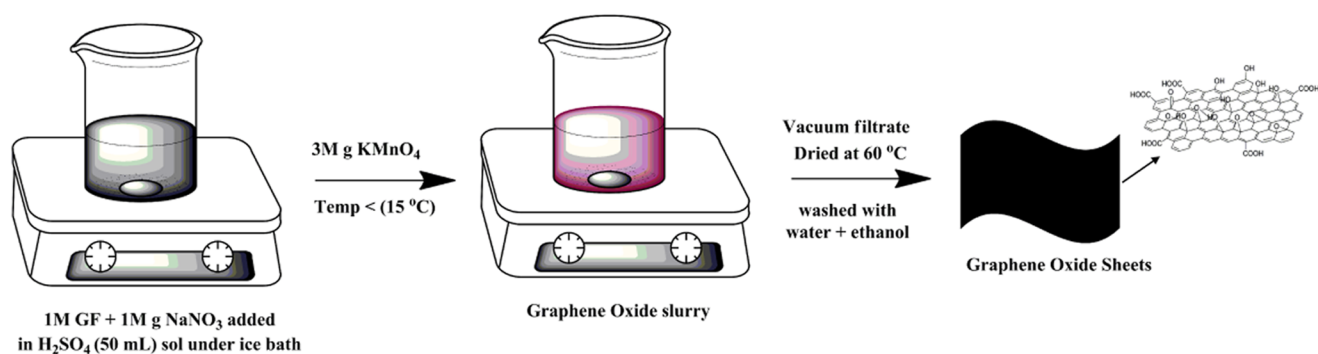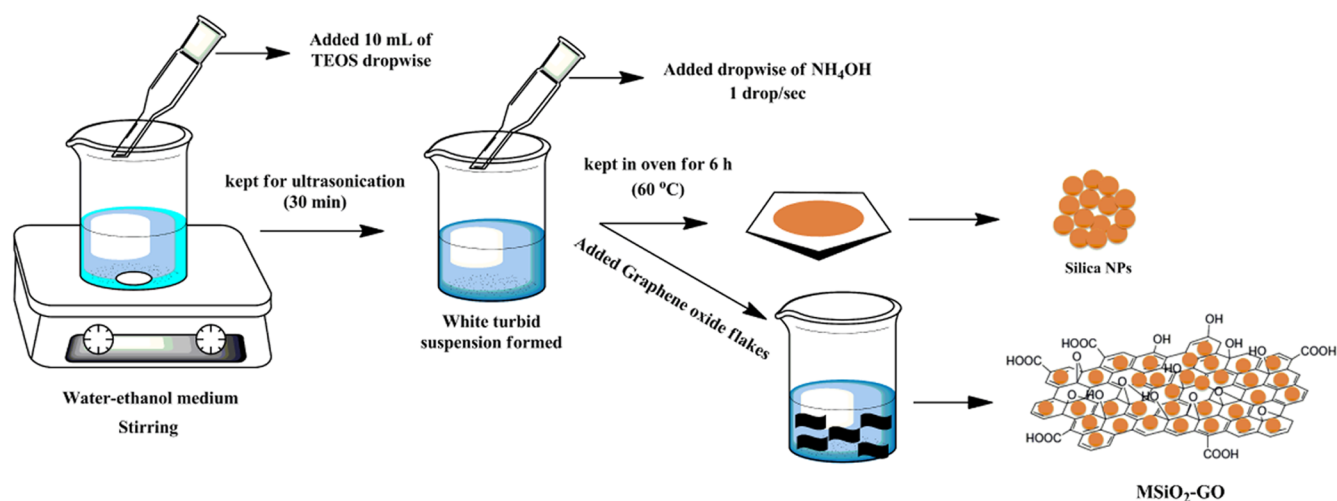
Figure 1. Synthesis process of GO sheets (1st step) and MSiO$_2$ NPs and MSiO$_2$-GO nanosheets (2nd step).

The incorporation of nanoparticles into the GO layer prevented not only useful aggregation of single GO sheets but also that of nanoparticles themselves.[9] Besides, GO-based composites with a more massive surface area show excellent properties compared to bare nanoparticles due to the interactive effect of nanoparticles and graphene sheets.

In the present study, silica nanoparticles have been used for intercalation in GO sheets since they offer certain advantages, such as low cost, innocuity, easy availability, chemical stability, biocompatibility, large specific surface areas, uniform pore size, and reproducibility.[3,9] However, one of the practical disadvantages of using the nanoparticles alone for the treatment of water from heavy metals is that it is difficult to strip out nanoparticles from the aqueous solution after treatment.[14] This assumes critical importance in applications such as heavy metal removal from water where regeneration of the adsorbent is necessary. The nanoparticle-inoculated GO sheet, on the other hand, is quite easy to strip out from water.[1,9,14,15]

Thus, in the present work, silica NPs were embedded in the GO layer to decrease the folding nature of GO sheets, thereby increasing its mechanical strength. Herein, mesoporous silica nanoparticles decorated with GO sheets (MSiO$_2$-GO) were synthesized and then applied as sorbents for the effective elimination of lead ions from water. It has been reported in the literature that nanoparticles have toxic and inflammatory effects on living cells.[16] This demands the cytotoxicity test of nanoparticles before they are applied to the exclusion of metal ions from water. Thus, the cytotoxicity test of MSiO$_2$-GO nanosheets was investigated on the Murine cells before incorporating it into the water.

2. SYNTHESIS OF THE GO/SIO$_2$ COMPOSITE

2.1. Materials. The chemicals along with their purity used for the synthesis of GO sheets and SiO$_2$ nanoparticles are listed here: (i) tetraethyl orthosilicate (TEOS, 98.0%, Sigma-Aldrich), (ii) ammonium hydroxide (NH$_4$OH) (28−30%), ethanol (99.5%), hydrochloric acid (HCl, 1 M), and sodium hydroxide (NaOH, 1 M) (all AR grade, Thermo Fisher Scientific, India), (iii) lead nitrates [Pb(NO$_3$)$_2$] (99.0%) purchased from Thomas Baker (Chemicals), India, (iv) potassium permanganate (KMnO$_4$) (99%, RFCL), sodium nitrate (NaNO$_3$) (98%, Nice Chemicals), graphite flakes (acid treated 99%, Asbury Carbons), hydrogen peroxide (H$_2$O$_2$) (40 wt %, Emplura), hydrochloric acid (HCl) (35%, RANKEM), and sulfuric acid (H$_2$SO$_4$) (98%, ACS), and (v) 6-diamidino-2-phenylindole dihydrochloride (DAPI), rhodamine phalloidin, and 4′

procured from Invitrogen, phosphate buffered saline (PBS) and paraformaldehyde procured from HI Media, Dulbecco's modified Eagle medium (DMEM) from Gibco, and Raw 264.7 cells from NCCS, Pune. The entire chemicals and reagents were used as received without further purification.

2.2. Synthesis of GO Sheets. GO sheets were prepared via the modified Hummers' method through the oxidation of graphite flakes.[17] Initially, 2 g each of graphite flakes and sodium nitrate was dissolved in H_2SO_4 (50 mL) in a volumetric flask kept in an ice bath (0−5 °C) with constant stirring for 2 h. Simultaneously, 6 g of $KMnO_4$ was added to the suspension slowly while maintaining the reaction temperature at <15 °C. After that, the ice bath was removed from the suspension, and the solution was stirred further at 35 °C until it turns to pasty brownish. The suspension was then diluted slowly by the addition of 100 mL of distilled water. The temperature of the reaction rises rapidly to 98 °C, turning the color of the suspension to brownish. The solution was further diluted by adding 200 mL of distilled water with continuous stirring. To terminate the reaction, 10 mL of H_2O_2 was added. The yellow color appeared, signifying the termination of the reaction. Finally, the mixture was washed several times via centrifugation using 10% HCl and distilled water several times. The final suspension was then vacuum-filtered by using a 1:1 volume ratio of water and ethanol. The obtained product was kept for drying in an oven at 40 °C. GO nanosheets were ground and collected in the powder form. The synthesis steps of graphene oxide nanosheets are displayed in Figure 1 (1st step).

2.3. Synthesis of MSiO$_2$ NPs. Mesoporous uniform-sized silica nanoparticles ($MSiO_2$ NPs) were synthesized by hydrolysis of TEOS in water−ethanol emulsion medium along with the ammonium hydroxide as reported in our earlier work.[18] First, 30 mL of water−ethanol medium (10 mL of water + 20 mL of ethanol) was kept for 30 min in an ultrasonication bath. Simultaneously, 10 mL of TEOS was added dropwise to the ultrasonication process. At the same time, 25% of NH_4OH was added dropwise to endorse the condensation of the reaction. Ultrasonication was further continued for 60 min to obtain a turbid white suspension. The fluid segment was separated by vacuum filtration and washed five times with ethanol/water medium (1:2 ratios). The remaining substantial portions were dried in an oven for 6 h at 60 °C and appropriately ground. Figure 1 (2nd step) shows an experimental procedure for the synthesis of uniformly sized mesoporous silica NPs. Below the reaction is the formation of $MSiO_2$ NPs.

$$\text{1st step:} \quad \text{Si-(OR)}_4 + H_2O \leftrightarrow \text{Si-(OH}_4) + 4\text{R-OH}$$
$$\text{(hydrolysis)} \tag{1}$$

$$\text{2nd step:} \quad 2\text{Si-(OH)}_4 \rightarrow 2(\text{Si} - \text{O} - \text{Si}) + 4H_2O$$
$$\text{(condensation)} \tag{2}$$
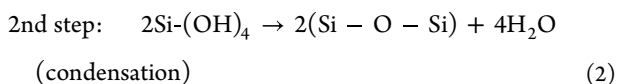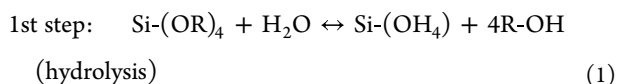
2.4. Synthesis of Nanosorbent MSiO$_2$-GO Nanosheets.
$MSiO_2$-GO nanosheets were prepared by dispersing 0.4 g of silica nanoparticles in 30 mL of ethanol and stirring for 1 h. Simultaneously, 0.2 g of GO sheets was added to aqueous silica, and the mixture was stirred for 1 h. The suspension was then placed for 30 min for ultrasonication to get the proper dispersion. Finally, the suspension was vacuum-filtered, and the residue was washed five times using ethanol−water medium. The obtained solid product was dried in an oven at 60 °C and

appropriately ground. Figure 1 (2nd step) displays the detailed synthesis of the $MSiO_2$-GO nanosheets.

2.5. Characterization of Nanosorbent MSiO$_2$-GO Nanosheets. *2.5.1. X-ray Diffraction (XRD) Analysis.* The structure, crystallinity, composition, and phase of the prepared GO nanosheets, $MSiO_2$ NPs, and $MSiO_2$-GO sheets were obtained using an analytical system diffractometer (model: DY-1656) using Cu Kα (λ = 1.542 Å).

2.5.2. High-Resolution Transmission Electron Microscopy (HRTEM) Analysis. To observe the size and surface morphology of the prepared nanoparticles, HR-TEM using a JEOL-2100 F (Japan) was used. Samples were prepared by dispersing a pinch of NPs in ethanol medium and ultrasonicated. Then, it was drop-cast on copper grids and kept for drying at room temperature.

2.5.3. Field Emission Scanning Electron Microscopy (FE-SEM) Analysis. The surface texture, morphology, and stage of aggregation were investigated via FESEM, Te-scan Model LYRA 3 XMU.

2.5.4. Fourier Transform Infrared (FTIR) Analysis. The surface composition of the prepared nanosorbents and the vibrational state of the adsorbed molecules were confirmed by using FTIR spectroscopy (Varian 7000). The sample for characterization was prepared by the KBr pellet method.

2.5.5. ζ-Potential Analysis. The surface potential of the synthesized nanosorbents was obtained from the measurement of the ζ-potential (model ZC-2000, Microtech, Japan). The small amount of NPs was dispersed in distilled water to prepare samples. The solutions were diluted to determine the surface charge of streaming particles.

2.5.6. BET (Brunauer−Emmett−Teller) Surface Area and Pore Size. The BET surface area and pore size of the synthesized NPs were obtained by using a Quanta chrome analyzer (model Autosorb-1). A 0.15 g amount of NPs was degassed at 200 °C for 6 h.

2.5.7. Atomic Absorption Spectrometry (AAS) Analysis. Lead ion detection in aqueous solution was determined through AAS, Savant AA, Australia. This technique is used for determining the concentration of particular elements (the analyte) in a sample.

2.6. In Vitro Cytotoxicity Test. The cells were treated with $MSiO_2$ NPs and $MSiO_2$-GO nanosheets and analyzed via a methyl-thiazole tetrazolium (MTT) assay to perform a cytotoxicity test. DMEM medium was used to culture macrophage cell lines (Raw 264.7) from Murine blood. The subconfluent flask cells were seeded into 96-well culture plates with 20×10^3 cells/well. Proper attachment of cells was achieved by incubating them overnight. Variable doses of $MSiO_2$/$MSiO_2$-GO nanosheets (5, 10, 20, 30, 40, and 50 μg mL^{-1}) were used to treat cells. The culture media were discarded after a period of 24 h, and subsequently, 0.5 mg mL^{-1} MTT solution was added to each well. Furthermore, the plates were incubated for 4 h to form formazan crystals; at the same time, crystals were dissolved in DMSO for 10 min. Absorbance was then taken at 570 nm using a microplate reader GMB-580. The cell viability % for each dose of $MSiO_2$/$MSiO_2$-GO nanosheets was measured, and a graph was plotted by using GraphPad Prism software (Graph Pad Software Inc.). All experiments have been carried out thrice.

2.7. Cell Morphology. The consequence of varying doses (5−50 μg mL^{-1}) of $MSiO_2$/$MSiO_2$-GO nanosheets on the cells' morphology was determined as described in detail elsewhere.[18] Treatment of cells was done separately using 40 μg mL^{-1} $MSiO_2$ and $MSiO_2$-GO nanosheets. Subsequently, after 24 h, the medium was discarded from each well and then kept for 20 min
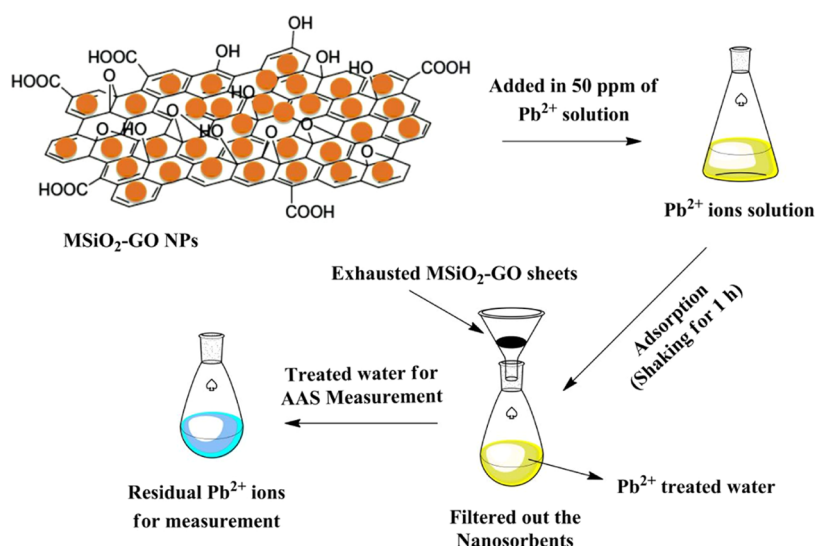
Figure 2. Stepwise process of Pb^{2+} ion adsorption onto MSiO$_2$-GO nanosheets.

at 4 °C with 4% paraformaldehyde. The staining of fixed cells was carried out by freshly prepared DAPI for the nucleus and rhodamine phalloidin for the cytoskeleton. Finally, with PBS (pH 7.4), the stained cells were washed two times and then mounted on glass slides. The morphological changes in MSiO$_2$/MSiO$_2$-GO-treated cells were observed through a fluorescence microscope (Nikon Eclipse Ti−S) by viewing glass sides.

2.8. Lead Ion Stock Solution Preparation. The stock solution of lead (Pb^{2+}) ions was prepared by adding 1 g of lead nitrates [Pb(NO$_3$)$_2$] in 1000 mL of distilled water. A drop (1−2) of concentrated nitric acid (HNO$_3$) was added as an analyte to keep the solution fresh.

2.9. Adsorption Experiments. Adsorption studies for Pb^{2+} ion removal by MSiO$_2$-GO nanosheets were conducted in batch mode. The effect of solution pH on Pb^{2+} adsorption was examined at varying pH values of 2.0−10.0. The solution pH was adjusted by using 1 M NaOH and HCl. The effects of contact time and NPs dose on Pb^{2+} sorption at various time intervals (2−30 min) and MSiO$_2$-GO dose (3−20 mg L^{-1}) were characterized. The sorption equilibrium studies were carried out at various temperatures (25, 35, and 45 °C) by dispersing MSiO$_2$-GO nanosheets (15 mg) in 50 mL of varying Pb^{2+} ion solutions (Pb^{2+} conc. = 10, 30, 50,80, 100, 120, 150 mg L^{-1}; shaking speed = 200 rpm for 1 h). Then, lead ion-treated water was filtered using Whatman 42 filter paper for the AAS measurement. The amount of Pb^{2+} adsorbed on MSiO$_2$-GO nanosheets per unit mass was calculated using eq 3. Lead adsorption % was calculated from eq 4

$$q_e = \frac{(C_i - C_e) \times V}{W} \tag{3}$$

$$S = \frac{(C_i - C_e)}{C_i} \times 100\% \tag{4}$$

q_e is the amount of Pb^{2+} adsorbed per gram of MSiO$_2$-GO nanosheets (mg g^{-1}), C_i and C_e are the initial and equilibrium concentrations (mg L^{-1}) of Pb^{2+} in solution, v is the volume (L), w is the weight (g) of the MSiO$_2$-GO nanosheets, and S is the adsorption percentage of Pb^{2+} ions. The stepwise process of adsorption studies of Pb^{2+} onto MSiO$_2$-GO nanosheets is illustrated in Figure 2.

3. RESULTS AND DISCUSSION

Figure 3 depicts the XRD patterns of (a) GO sheets; (b) MSiO$_2$ NPs; and (c) MSiO$_2$-GO nanosheets. The XRD pattern of
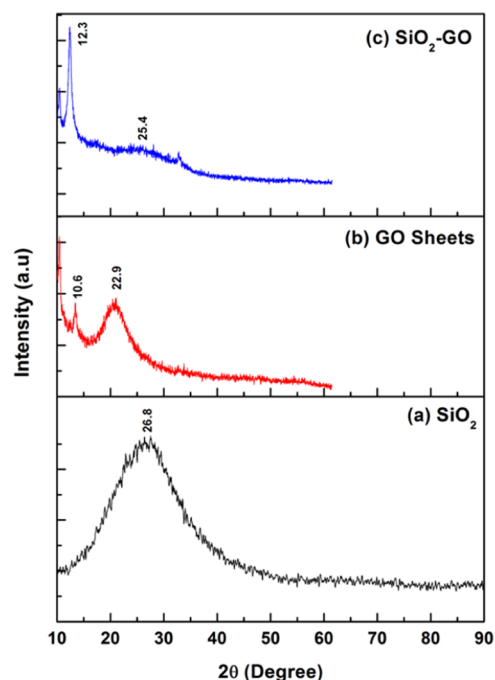
Figure 3. XRD patterns of (a) GO sheets; (b) MSiO$_2$ NPs; and (c) MSiO$_2$-GO nanosheets.

MSiO$_2$ NPs shows a board peak centered at 26.8°, which is attributed to the amorphous nature of silica nanoparticles.[19,20] GO sheets show two peaks at 10.6 and 22.9°, which are in conformity with the well-known XRD peak of GO.[20] In the case of the composite, MSiO$_2$-GO nanosheets, the peaks at 10.6 and 22.9° (GO sheets) and 26.8° (SiO$_2$ NPs) shifted to 12.4 and 25.4°. The shifted sharp peak at 12.4° corresponds to the presence of GO, while the broad peak around 25.4° is formed due to the intercalation of silica NPs in the GO sheet network.

TEM images of GO sheets and MSiO$_2$-GO nanosheets are shown in Figure 4a−f. The image (a) clearly shows the excellent
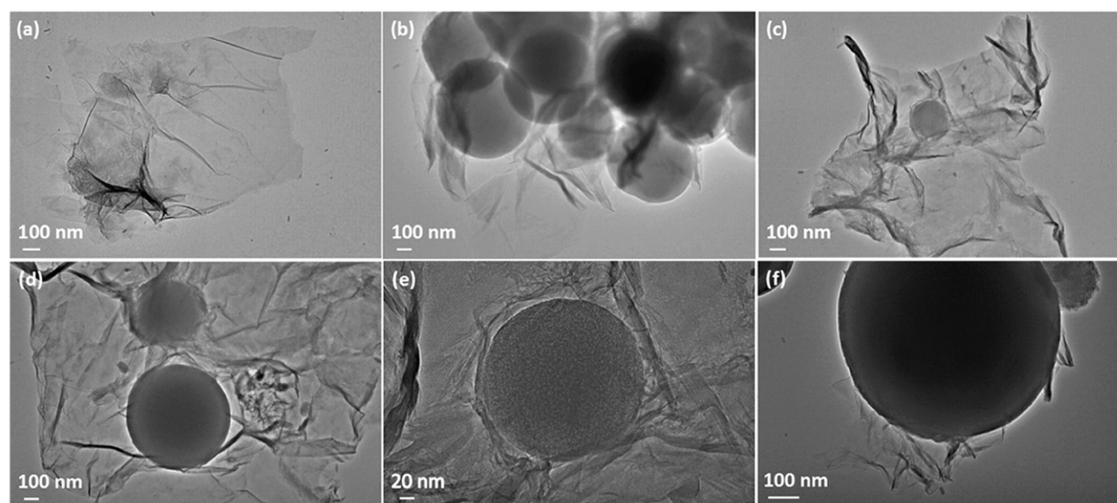
Figure 4. TEM images of different magnifications of (a) single layered GO sheets (1kx) and (b−f) $MSiO_2$-GO nanosheets (b) (8k×); (c) (1k×); (d) (1k×); (e) (5k×); and (f) (2k×).
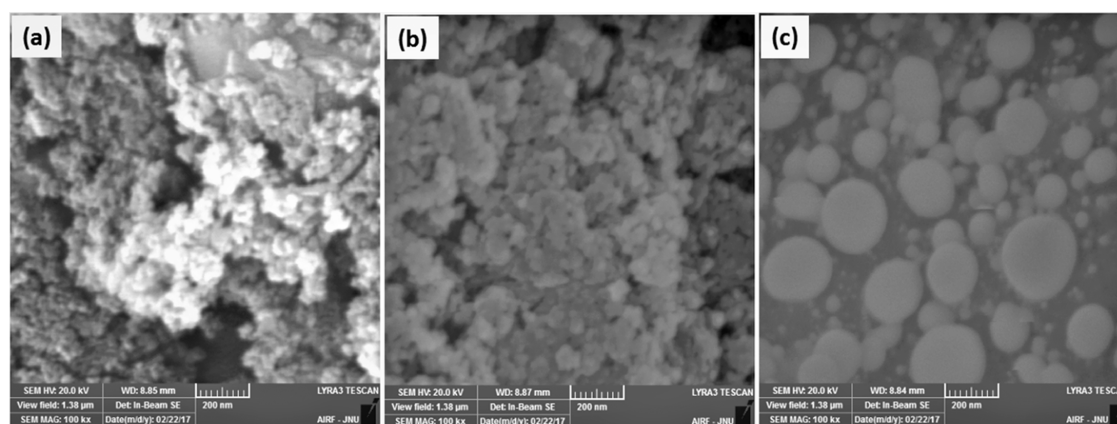
Figure 5. FE-SEM images of (a−c) $MSiO_2$-GO nanosheets.

formation of transparent single-layered GO sheets with tiny ripples. The images (b−f) depict uniform-sized spherical silica nanoparticles embedded onto the surface of GO layers. The obtained average size for $MSiO_2$ NPs is ∼70 nm. It appears from the images (b−f) that silica NPs are embedded on GO layers via van der Waals forces of attraction between the intermolecular forces of atoms. Image (b) shows a cluster of uniform-sized $MSiO_2$ NPs embedded on the GO sheets. However, image (d) shows two different sizes of dispersed silica NPs embedded in GO sheets. The shrinkage in particle size is due to the trivial ripple of graphene sheets.

Figure 5a−c shows the FE-SEM images of the $MSiO_2$-GO nanosheets. From images (a−c), the uniform distribution of silica nanoparticles on the surface of GO sheets is evident. It is also visible that the synthesized silica NPs are highly dispersed.

Figure 6 displays the FTIR spectra of GO sheets, $MSiO_2$ NPs, and $MSiO_2$-GO nanosheets. A wideband appears at 3429 cm^{-1} in all the spectra because of O−H stretching vibration, which is due to the presence of ambient moisture in the compounds [Figure 6a−c]. Due to extensive oxidation, GO sheets have IR peaks at 1720, 1637, and 1104 cm^{-1}, which are attributed to the carboxyl C=O stretching band, O−H deformation vibration band, and C−O stretching vibration, respectively [Figure 6a].[9,20] A band appearing at 2927 cm^{-1} is due to the C−H stretching mode from the carboxylic group. A peak at 1104 cm^{-1}
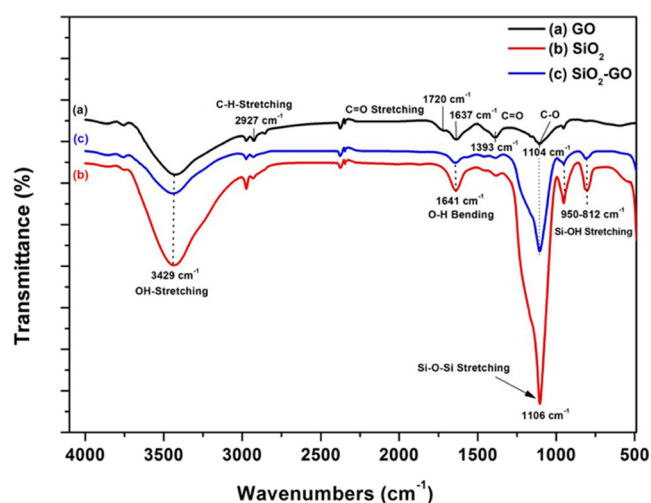
Figure 6. FTIR spectra of (a) GO sheets; (b) $MSiO_2$ NPs; and (c) $MSiO_2$-GO nanosheets.

ascertained in GO responds to the C−O stretching vibration from the alkoxide group and the C−O stretching vibration at 1393 cm^{-1} corresponds to the carboxyl group.[20−22]

The IR peaks of silica NPs show three sharp peaks: One at 1106 cm^{-1}, which is due to the antisymmetric stretching

vibration of Si−O−Si. The second IR band observed at 950 cm^{-1} is allotted to the Si−OH stretching vibration.[20−22] The third IR band at 812 cm^{-1} is due to the symmetric stretching vibration of Si−O−Si [Figure 6b].[23−25]

However, FTIR peak intensity of the composite MSiO$_2$-GO nanosheets of the Si−O−Si band (1104 cm^{-1}) shows significant increases in comparison to GO sheets while decreases as compared to silica NPs, which could be attributed to the reduction of the native oxide [Figure 6a,c]. The peak intensity of other carboxyl groups decreases as compared with GO sheets. Thus, it is an illustration of the successful formation of MSiO$_2$-GO nanosheets. Table 1 illustrates the FT-IR spectra and functional groups of GO sheets, SiO$_2$ NPs, and composite MSiO$_2$-GO nanosheets.

Table 1. FTIR Absorbance Spectra of GO Sheets, MSiO$_2$ NPs, and Composite MSiO$_2$-GO Nanosheets

materials	wavenumber (cm^{-1})	types of functional groups
GO sheets	3429	O−H stretching vibration
	2927	C−H stretching mode of the carboxylic group
	1720	C═O stretching vibration of the carboxyl group
	1637	O−H deformation−vibration
	1393	C−O stretching vibration of the carboxyl group
	1104	C−O stretching vibration of the alkoxide group
SiO$_2$	3429	O−H stretching vibration
	1641	O−H bending vibration
	1106	Si−O−Si stretching vibration
	950	Si−OH stretching vibration
	812	Si−O−Si bending vibration

UV−visible absorbance spectra of MSiO$_2$ NPs, GO sheets, and MSiO$_2$-GO nanosheets are shown in Figure 7a−c. Bare silica NPs show an absorption band at 203 nm. Two sharp characteristic absorption bands appeared at 200.2 and 220.8 nm in the UV−visible spectra of GO nanosheets [Figure 7b]. The absorption band at 200.2 nm is assigned to $\varrho \rightarrow \varrho^*$ aromatic C−C bond transitions. A sharp peak at 220.8 nm is attributed to
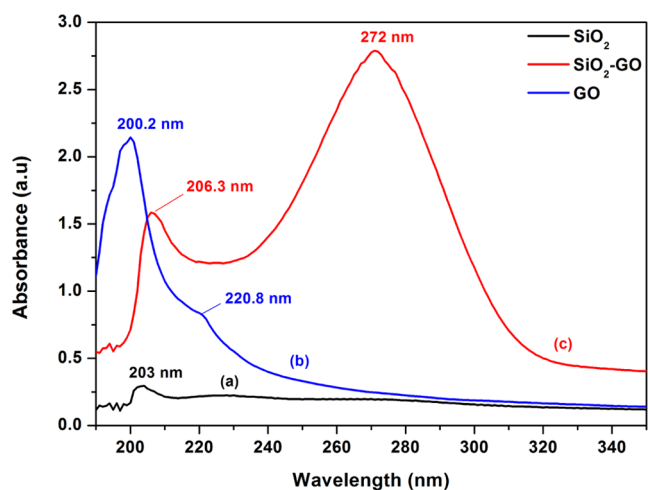
Figure 7. UV absorbance spectra of (a) MSiO$_2$ NPs; (b) GO sheets; and (c) MSiO$_2$-GO nanosheets.

$n \rightarrow \varrho^*$ transitions of C═O bonds.[8,20,26,27] The absorbance band of the composite MSiO$_2$-GO nanosheets in the whole spectra increases, which is evident from the red shift of the absorption peak of GO sheets at 200.2 and 220.8 nm to 206.3 and 272 nm, respectively [Figure 7c].[23,25,26] These shifts of bands could be due to the absorption of surface-attaching MSiO$_2$ NPs.

Furthermore, the red shift of MSiO$_2$-GO nanosheet spectra is due to the close conjugation of MSiO$_2$ NPs and the GO sheets that results in rapid electron transfer and increased transition energy.[8,25]

Figure 8(i) depicts the obtained surface ζ-potential of GO sheets, MSiO$_2$ NPs, and composite MSiO$_2$-GO nanosheets dispersed in distilled water (neutral pH 7.0). The surface potential of GO sheets was obtained to be −18.5 mV. The profoundly negative ζ-potential of GO sheets is due to the hydroxyl group (−OH$^-$) and the carboxyl group (−COO$^-$) present in GO. The obtained ζ-potential of silica NPs was found to be +32 mV; the positive surface is due to the acidic nature of silica NPs, which enhances the hydronium ions (H$^+$). However, the embedding of SiO$_2$ NPs onto GO sheets makes the surface negatively charged (ζ-potential = −12 mV) due to the presence of GO functional groups −OH$^-$ and −COO$^-$, respectively.[28,29]

To obtain the point zero charge (pHpzc) of MSiO$_2$-GO nanosheets, ζ-potential analysis was performed at different pH values varying from 1 to 10 adjusted using 0.01 M NaOH and 0.01 M HCl. The samples were prepared by dispersing a trace amount of NPs in 10 mL of distilled water, followed by agitation for 6 h. Figure 8(ii) shows a typical plot of ζ-potential versus pH value varying from 1 to 10. The obtained ζ-potential charges for pH 1−10 were 0.0 mV (pH 1), −32 mV (pH 2), −40.7 mV (pH 3), −39.1 mV (pH 4), −36.6 mV (pH 5), −43.9 mV (pH 6), −49.7 mV (pH 7), −45 mV (pH 8), −53.5 mV (pH 9), and −49.3 mV (pH 10). The pHpzc value of MSiO$_2$-GO NPs was obtained at an aqueous pH of 1.0 (±0.0 mV). The negative ζ-potential of MSiO$_2$-GO nanosheets is due to the ionization of the carboxyl group (−COO$^-$) present in GO.[28,29]

3.1. Cytotoxicity Studies. Figure 9a shows the comparative *in vitro* cytotoxicity studies of MSiO$_2$ NPs and MSiO$_2$-GO nanosheets in relative percentage proliferation/survival of the macrophage normal Raw 264.7 cell line from Murine blood treated with MSiO$_2$/MSiO$_2$-GO nanosheet concentration (5−80 μg mL^{-1}). It is clear from the plot that cell viability remains unaltered in MSiO$_2$/MSiO$_2$-GO nanosheet-treated cells compared with untreated cells.

Figure 9b(ii,iii) shows the fluorescence microscopy images of cells treated with 40 μg mL^{-1} MSiO$_2$/MSiO$_2$-GO nanosheet concentration incubated for 24 h. The cellular morphology of untreated cells and DAPI-stained nuclei of MSiO$_2$/MSiO$_2$-GO nanosheets treated cells were the same, implying no observable changes in treated cells. Even at a higher dose (40 μg mL^{-1}) of MSiO$_2$/MSiO$_2$-GO nanosheets, the microscopic images show a negligible change in cell morphology. Thus, both MSiO$_2$ NPs and MSiO$_2$-GO nanosheets do not show any adverse effect on cell viability, thereby indicating high biocompatibility of the synthesized MSiO$_2$-GO nanosheets.

BET surface area and pore size distribution of MSiO$_2$ and MSiO$_2$-GO nanosheets were obtained by measuring N$_2$ adsorption and desorption. N$_2$ adsorption studies were conducted by degassing the sample under vacuum at 200 °C for 6 h. Figure 10 shows the N$_2$ adsorption−desorption isotherm curve, which is a typical Type IV isotherm and displays a type H$_2$ hysteresis loop.[30] The obtained BET surface areas of MSiO$_2$
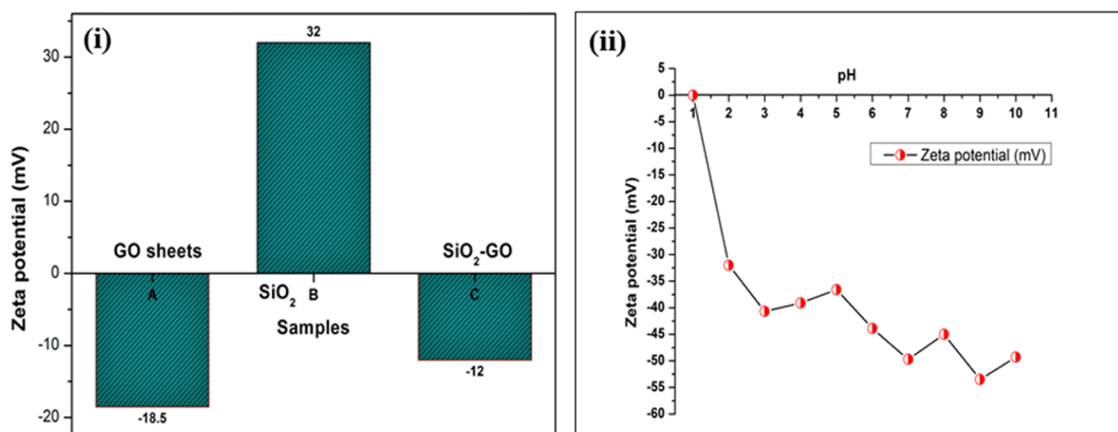
Figure 8. (i) ζ-potential plots of (sample A) GO sheets; (sample B) MSiO$_2$ NPs; and (sample C) MSiO$_2$-GO nanosheets. (ii) Point zero charge (pHpzc) of MSiO$_2$-GO nanosheets.
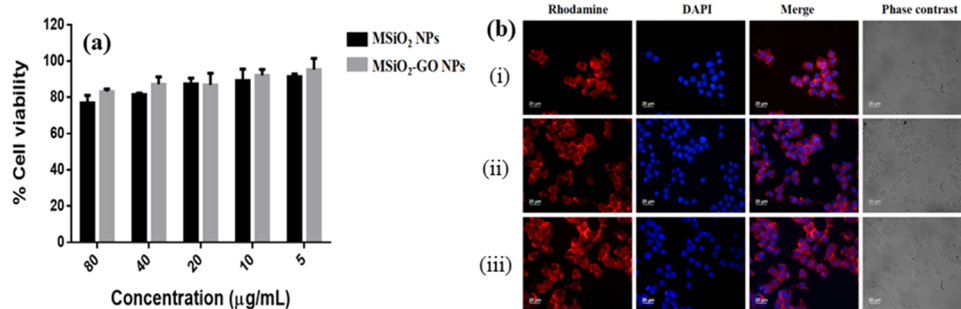
Figure 9. (a) MTT assay to determine the cell viability of the Raw 264.7 cells at varying concentrations of MSiO$_2$ and MSiO$_2$-GO nanosheets. (b) Fluorescence microscopy images of Raw 264.7 cells treated with MSiO$_2$ and MSiO$_2$-GO: (i) untreated cells; (ii) 40 μg mL^{-1} MSiO$_2$ NPs; and (iii) 40 μg mL^{-1} MSiO$_2$-GO. Images were captured at 40x using a fluorescence microscope (Nikon Eclipse Ti−S).
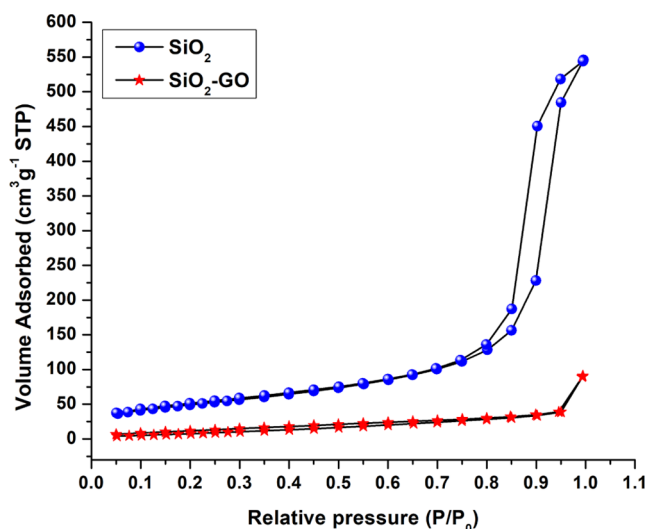
Figure 10. N$_2$ adsorption−desorption isotherm plots of MSiO$_2$ and MSiO$_2$-GO nanosheets.

NPs and MSiO$_2$-GO nanosheets were 177.597 and 40.239 m^2 g^{-1}, respectively. The average pore diameter and pore volume were determined from the distribution (PSD) curve using the Barrett−Joyner−Halenda (BJH) method. The pore diameter was obtained as 30.693−17.726 nm for MSiO$_2$ NPs and 15.282−19.112 Å for MSiO$_2$-GO nanosheets, respectively. The obtained results indicate that both the NPs were mesoporous.[30] The total pore volume was obtained as 0.850−0.853 cm^3 g^{-1} for

MSiO$_2$ and 0.139−0.126 m^2 g^{-1} for MSiO$_2$-GO. It is clear from comparative Table S1 that the BET surface area, pore volume, and pore size of MSiO$_2$ NPs reduced after being embedded in GO sheets. This is because some pores of MSiO$_2$ NPs are partly enclosed after being assorted with graphene sheets, thereby reducing the pore size, pore volume, and surface area. Similar results were reported earlier in the literature.[30,31]

3.2. Adsorption of Lead Ions at Different Parameters. The comparative lead adsorption studies of bare MSiO$_2$ NPs and GO-MSiO$_2$ nanosheets were performed using 15 mg L^{-1} NP dose dissolved in 50 mg L^{-1} Pb solution at optimal parameters (temp.: 25 °C; shaking speed: 200 rpm; pH: 6.0). It is clear from Figure 11 that both the nanosorbents successfully adsorbed Pb^{2+} ions from water. The removal efficiency of Pb^{2+} ions using the adsorbent GO-MSiO$_2$ is significantly higher compared with bare MSiO$_2$ NPs. About 90.4% of Pb^{2+} ions were adsorbed using GO-MSiO$_2$, and 71.5% were adsorbed using bare MSiO$_2$ NPs. The better adsorption of lead ions using GO-MSiO$_2$ is due to the graphene sheet's excellent properties, such as large surface area, high mobility of charge carriers, and chemical stability. Furthermore, GO sheets contain several functional groups, such as hydroxyl (−OH), carboxyl (−COOH), and epoxy groups (−C═O). These functional groups enhance the excellent adsorption sites for Pb^{2+} ions in water. Thus, GO-MSiO$_2$ nanosheets have been used as sorbents for the rest of the adsorption parameters.

3.2.1. Effect of the Nanosorbent Dose. To find out the optimal dose of MSiO$_2$-GO nanosheets on adsorption of Pb^{2+} ions, the experiment was conducted at various adsorbent doses
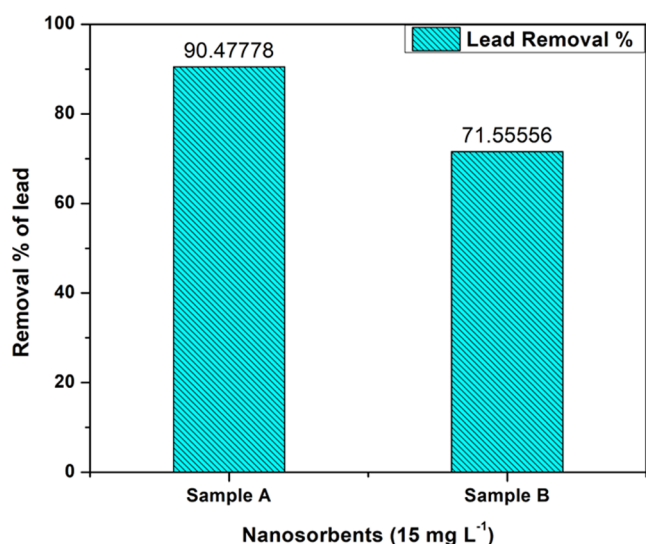
Figure 11. Comparative lead adsorption using nanosorbent $MSiO_2$-GO nanosheets (sample A) and $MSiO_2$ NPs (sample B).

(3, 5, 10, 15, 20 mg L^{-1}) in 50 ppm Pb^{2+} ions with certain optimum conditions (temperature: 25 °C; equilibrium time: 60 min; shaking speed: 200 rpm). Figure 12 shows the effects of
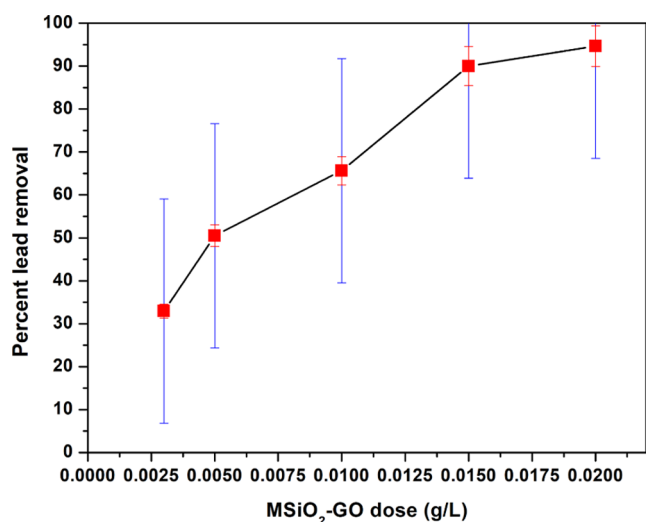
Figure 12. Effect of $MSiO_2$-GO nanosheet doses on adsorption of Pb^{2+} ions.

Pb^{2+} absorption with various doses of $MSiO_2$-GO nanosheets. It could be understood from the plots that the removal efficiency of Pb^{2+} ions significantly increases with the increase in the doses of the $MSiO_2$-GO nanosheets. About 25−90% lead removal was obtained at the dose of 3−20 mg L^{-1}. This is because the increase in adsorbent doses increases the available adsorption sites, which leads to more binding of Pb^{2+} ions.[1,2,32] The maximum removal condition of Pb^{2+} ions has been obtained at an adsorbent dose of 15 mg L^{-1}, and after that, not much further removal occurred. Hence, a 15 mg L^{-1} dose of $MSiO_2$-GO nanosheets was taken in all the adsorption studies.

3.2.2. Effect of the Aqueous pH. The aqueous pH determines the effects of adsorbent surface charge, the degree of ionization, its functional groups, and the solubility of metal ions during the reaction between the adsorbent and adsorbate.[1,32] To analyze the effect of solution pH on the adsorption of Pb^{2+} ions onto the

$MSiO_2$-GO nanosheet surface, 15 mg L^{-1} adsorbent was added into 50 mL containing Pb^{2+} (50 mg L^{-1}) with adjusted pH (2.0− 10.0). NaOH and HCl solutions set the aqueous pH. The consequences of aqueous pH on Pb^{2+} ion adsorption in a pH range from 2.0 to 10.0 are shown in Figure 13. Lead ions start
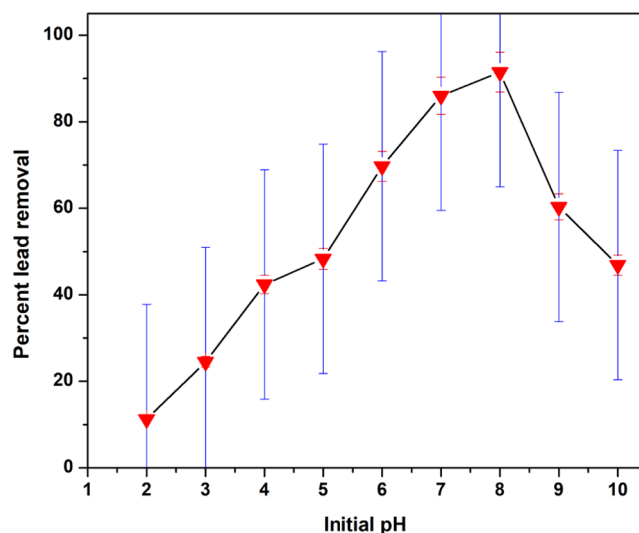
Figure 13. Effect of aqueous pH on the adsorption of Pb^{2+} ions onto $MSiO_2$-GO nanosheets.

precipitating from solution pH > 7.0. It is clear from the plot that at pH 2.0−3.0, the removal efficiency of the Pb^{2+} ion is almost unnoticed; however, the adsorption of Pb^{2+} increases rapidly as the solution pH rises from 4.0 to 7.0 due to an increase in the negative ζ-potential of $MSiO_2$-GO from −39.1 to −49.7 mV as shown in Figure 8(ii). This is due to less competition of active sites between hydrogen ions versus Pb^{2+} ions, which results from the negative surface charge of GO nanosheets obtained from −OH and −COOH functional groups, thereby resulting in more electrostatic attractions of Pb^{2+} ions and negative surface (−OH and −COOH) of $MSiO_2$-GO nanosheets.[33,34]

At basic pH, lead ions are positively charged species Pb^{2+} and $Pb(OH)^+$.[26,34] Therefore, the significant increase of Pb^{2+} adsorption at aqueous pH 3.0−7.0 is due to electrostatic attraction of highly negative surface charge of $MSiO_2$-GO nanosheets and positive species Pb^{2+} and $Pb(OH)^+$ ions.[26,33] The functional groups of GO such as −OH and −COO$^-$ are progressively deprotonated when the pH increases.

At low solution pH (2.0−3.0), the adsorption of Pb^{2+} ions is low due to the competition between Pb^{2+} ions and hydrogen ions (H^+), resulting in a repulsion of both ions.[26,33] Furthermore, at low pH, $MSiO_2$-GO nanosheet surfaces have a high positive charge that leads to electrostatic repulsion with Pb^{2+} ions, which results in a low adsorption. The probable reaction mechanism of Pb^{2+} ion sorption onto $MSiO_2$-GO nanosheets is shown in Figure 14.

3.2.3. Effect of the Time Interval and Adsorption Kinetics. To monitor the consequence of interaction time on the adsorption of Pb^{2+} onto $MSiO_2$-GO nanosheets, the studies were conducted at diverse time intervals between 2 and 30 min at optimum conditions (pH: 6; $MSiO_2$-GO dose: 15 mg L^{-1}; Pb^{2+} ions conc.: 50 mg L^{-1}; temp.: 25 °C; shaking speed: 200 rpm). It is evident from Figure 15 that the adsorption efficiency of Pb^{2+} ions increases from 30 to 98% with the rise of the interaction time interval from 2 to 30 min.[1,26] About 75% of Pb^{2+}
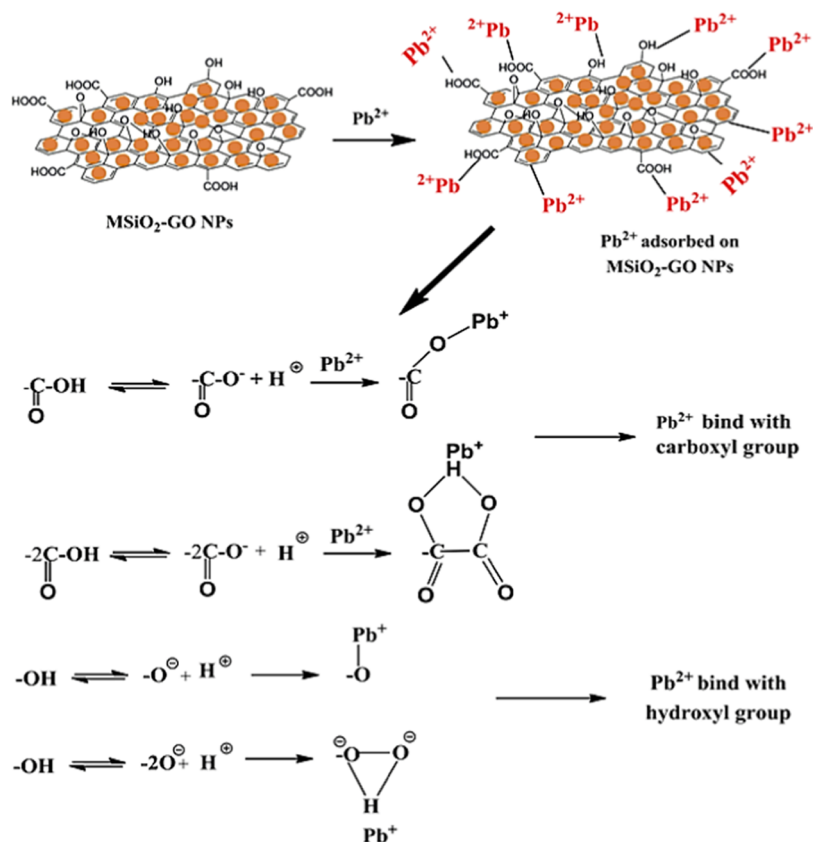
Figure 14. Possible reaction mechanism of Pb^{2+} ion sorption onto $MSiO_2$-GO nanosheets.
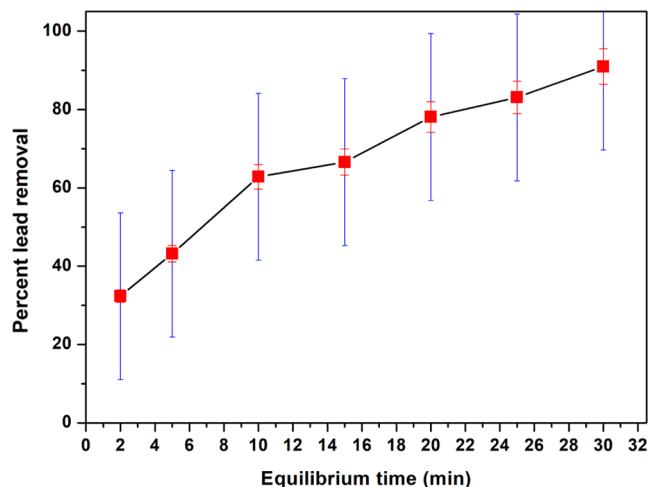
Figure 15. Effect of the time interval on the adsorption of lead onto $MSiO_2$-GO nanosheets.

ion uptake occurs within 10 min, and 98% occurs within 25 min. In both cases, the adsorption rate at the beginning is fast and then slows down as the equilibrium is achieved. The adsorption equilibrium for both Pb^{2+} adsorptions was achieved in nearly 25−30 min. The sorption kinetic pseudo-first- and pseudo-second-order models were applied to investigate the absorption mechanism between Pb^{2+} ions and $MSiO_2$-GO nanosheets, including chemical reaction, mass transfer, and potential of rate control. Equations 5 and 6 describe the linear expressions of pseudo-first- and pseudo-second-order kinetic rates.

$$\log(q_e - q_t) = \log(q_e) - \frac{k_1 t}{2.303} \tag{5}$$

$$\frac{t}{q_t} = \frac{1}{k_2 q_e^2} + \frac{t}{q_e} \tag{6}$$

k_1 and k_2 (min^{-1}) are the adsorption first-order and second-order rate constants, respectively, and q_e, and q_t ($mg\,g^{-1}$) are the amounts of Pb^{2+} adsorbed at equilibrium and at time t, respectively.

Figure 16a,b shows the pseudo-first- and pseudo-second-order kinetic plots examined for Pb^{2+} adsorption by $MSiO_2$-GO nanosheets. The equilibrium adsorption amount for Pb^{2+} is calculated using eqs 5 and 6. The obtained Pb^{2+} adsorption q_e onto $MSiO_2$-GO nanosheets for pseudo-first and pseudo-second order is 72.276 and 111.12 $mg\,g^{-1}$, respectively. The determination coefficient factor (R^2) and kinetic rate constants (k_1 and k_2) have been calculated from the graphical plot intercepts and slopes.

The calculated kinetic parameters are presented in Table 2. The acquired values of R_1^2 from pseudo-first-order and R_2^2 pseudo-second-order for Pb^{2+} sorption are 0.982 and 0.983, respectively, which are almost the same. The adsorption data of Pb^{2+} ions are fitted well with both pseudo-first- and pseudo-second-order kinetic models, indicating adsorption of Pb^{2+} onto the $MSiO_2$-GO surface to be chemisorption as well as physisorption. Related remarks have been reported earlier.[26]

3.3. Lead Adsorption Isotherms. The adsorption isotherm models Langmuir and Freundlich have been used to better understand the adsorption mechanism of Pb^{2+} ion and $MSiO_2$-GO nanosheet interaction. The Langmuir isotherm states monolayer adsorption of metal ions on the surface of the
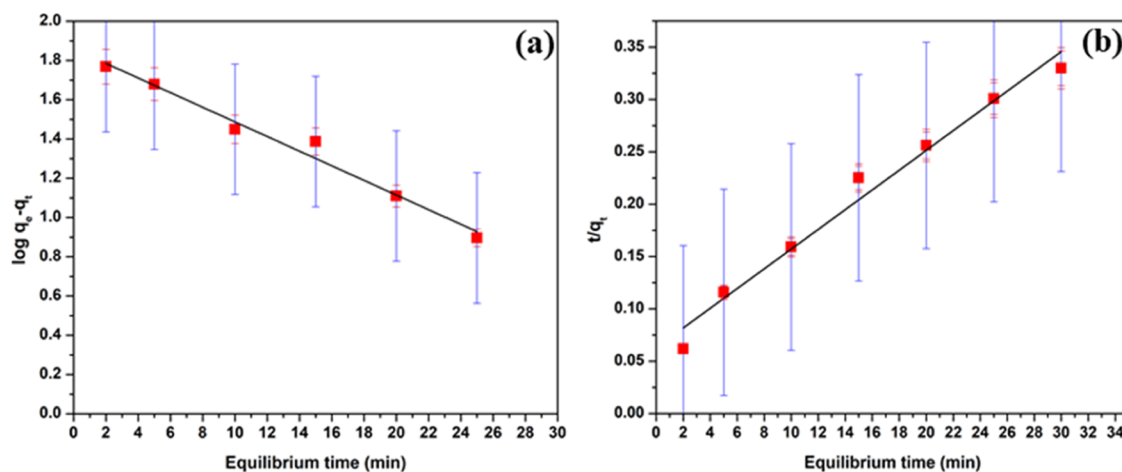
Figure 16. (a) Pseudo-first-order kinetic plot on adsorption of Pb^{2+} onto $MSiO_2$-GO nanosheets. (b) Pseudo-second-order kinetic plot on adsorption of Pb^{2+} onto $MSiO_2$-GO nanosheets.

Table 2. Kinetic Model Parameters of Pb^{2+} Adsorption on $MSiO_2$-GO Nanosheets

parameters	pseudo-first-order	pseudo-second-order
slope (m)	−0.037	0.009
K	0.436	0.001
intercept (c)	1.859	0.062
q_e (mg g^{-1})	72.27	111.12
R^2	0.982	0.983

adsorbent with uniform energy. However, the Freundlich isotherm suggested the multilayer sorption of metal ions on the adsorbent surface via the nonuniform distribution of energy. The value of "$1/n$" represents the degree of nonlinearity between adsorption and solution concentration. Adsorption is linear when $n = 1$, chemical adsorption when $n < 1$, and physical adsorption when $n > 1$.

Similarly, R_L is the Langmuir adsorption isotherm parameter, which can be obtained using a dimensionless constant called the separation factor or equilibrium parameter by eq 7

$$R_L = \frac{1}{(1 + bC_i)} \tag{7}$$

where C_i stands for the initial concentration and b stands for the Langmuir constant. Adsorption should be irreversible when $R_L = 0$, linear when $R_L = 1$, unfavorable when $R_L > 1$, and favorable adsorption when $0 < R_L < 1$.

The isotherm models Langmuir and Freundlich for Pb^{2+} sorption on $MSiO_2$-GO nanosheets at different temperatures (25−45 °C) are shown in Figures 17 and 18. The obtained Langmuir correlation values (R^2) for the adsorption of Pb^{2+} at different temperatures (25, 35, and 45 °C) are 0.912, 0.305, and 0.989, respectively. The Freundlich correlation values (R^2) are found to be 0.869, 0.856, and 0.833, respectively. The obtained Langmuir and Freundlich adsorption parameters are listed in Table 3. The Langmuir correlation factor "R^2" is found to be better than the value of the Freundlich model, indicating the monolayer adsorption of Pb^{2+} on $MSiO_2$-GO nanosheets. The Langmuir separation factor "R_L" for Pb^{2+} adsorption obtained is in the range of 0.1−0.9 [Figure 19]. In the present study, $R_L > 0$ indicates favorable adsorption of Pb^{2+} on $MSiO_2$-GO. The compared adsorption of Pb^{2+} on $MSiO_2$-GO nanosheets versus other nanosorbents is listed in Table S2.[6,21,35−41]
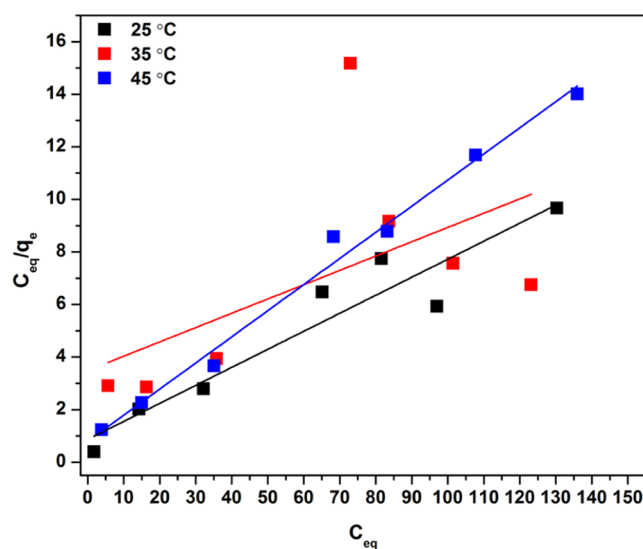
Figure 17. Langmuir isotherm plots on Pb^{2+} adsorption onto $MSiO_2$-GO nanosheets with varied temperatures (25−45 °C).
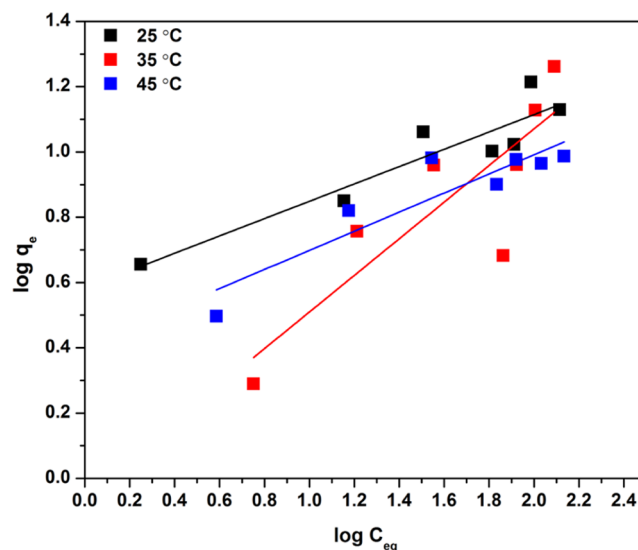
Figure 18. Freundlich isotherm plots on Pb^{2+} adsorption onto $MSiO_2$-GO nanosheets at varied temperatures (25−45 °C).

Table 3. Langmuir and Freundlich Isotherms Parameters

isotherm plots	temperature (°C)	m (slope)	q_{max} (mg g^{-1})	c (intercept)	b	R^2
Langmuir	25	0.068	14.706	0.867	0.078	0.912
	35	0.054	18.518	3.489	0.015	0.305
	45	0.099	10.101	0.793	0.124	0.989
isotherm plots	temperature (°C)	m (slope)	n	c (intercept)	K_F	R^2
Freundlich	25	0.266	3.75	0.584	3.83	0.869
	35	0.561	1.78	−0.052	1.12	0.856
	45	0.293	3.41	0.406	2.54	0.833
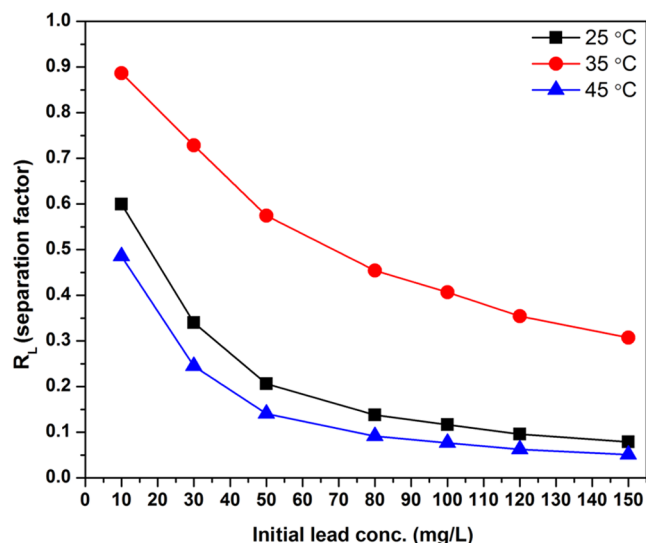
Figure 19. Langmuir separation factor (R_L) for Pb^{2+} adsorption onto MSiO$_2$-GO nanosheets at various temperatures (25−45 °C).

3.4. Confirmation of the Support of Pb^{2+} Adsorbed on MSiO$_2$-GO Nanosheets. Figure 20a,b displays the SEM/EDX spectra of MSiO$_2$-GO nanosheets and Pb^{2+}-loaded MSiO$_2$-GO, respectively. MSiO$_2$-GO nanosheets show distinctively visible spectra of elements such as silicon (34.68%), oxygen (61.11%), and carbon (4.21%) [Figure 20a]. Distinctly visible spectra of lead are shown in Figure 20b. This shows the elemental composition of lead (0.21%), thus confirming the adsorption of Pb^{2+} on the surface of MSiO$_2$-GO nanosheets.
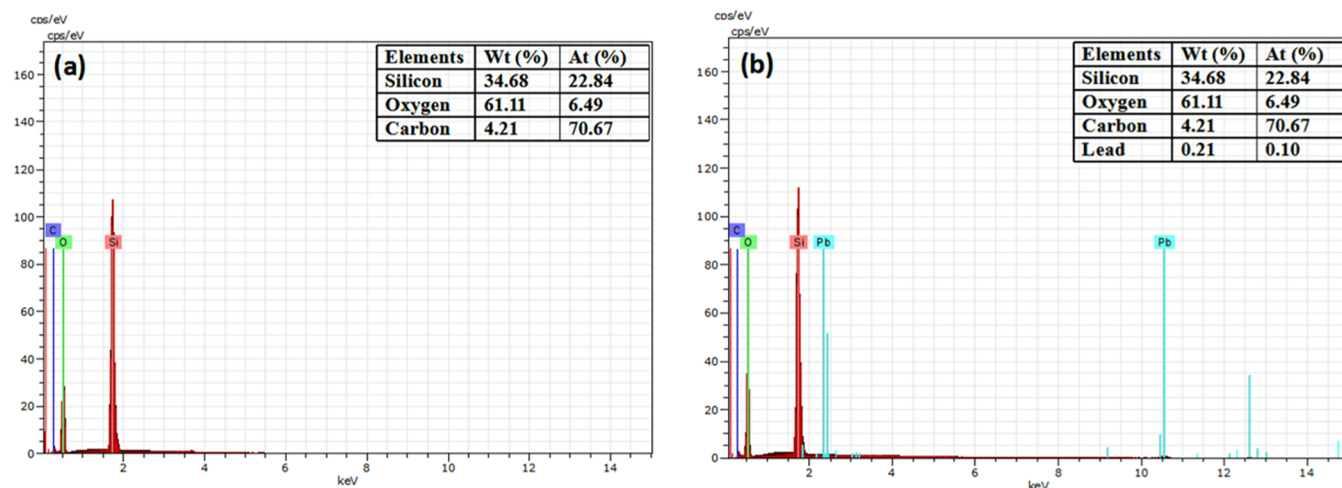
SEM elemental mapping analysis confirms the spatial distribution and elemental composition of lead onto MSiO$_2$-GO nanosheets, which illustrates the elements silica in red, oxygen in green, and carbon in royal blue [Figure 21a,b]. Image (c) visibly reveals a homogenous distribution of lead loaded on the surface of MSiO$_2$-GO nanosheets, which shows the composition of lead in yellow color.

3.5. Regeneration Studies of Exhausted MSiO$_2$-GO Nanosheets. The regeneration of exhausted MSiO$_2$-GO nanosheets was carried out by using 0.005 M HNO$_3$ as the desorbing agent. Initially, 0.1 g L^{-1} MSiO$_2$-GO was agitated with 50 mg L^{-1} Pb^{2+} solution for 60 min at 200 rpm shaking speed. The spent MSiO$_2$-GO was separated after Pb^{2+} adsorption and desorbed by using 0.005 M HNO$_3$ for five cycles. Figure 22 shows the regeneration plot for the MSiO$_2$-GO nanosheets. In the first aliquots (20 mL each), about 87% of the total recovered lead was desorbed, and the rest was desorbed in four increments of 20 mL of 0.005 M HNO$_3$.

4. CONCLUSIONS

Mesoporous silica-embedded graphene oxide (MSiO$_2$-GO) nanosheets were synthesized and characterized. MSiO$_2$ NPs embedded in the GO layer successfully decreased the folding nature of GO sheets as shown in TEM images, thereby increasing its mechanical strength. The comparative cytotoxicity studies of MSiO$_2$ NPs and MSiO$_2$-GO nanosheets reveal no change in cell morphology even at a high dose of NPs, thus showing excellent biocompatibility. About 90% of Pb^{2+} ions were detached from water within 30 min at solution pH 6.0. Sorption dynamic data agreed well with pseudo-first- and pseudo-second-order kinetic models, which indicates both physisorptions as well as chemisorptions and controlled

Figure 20. EDX spectra of (a) MSiO$_2$-GO nanosheets and (b) lead uptake MSiO$_2$-GO nanosheets.
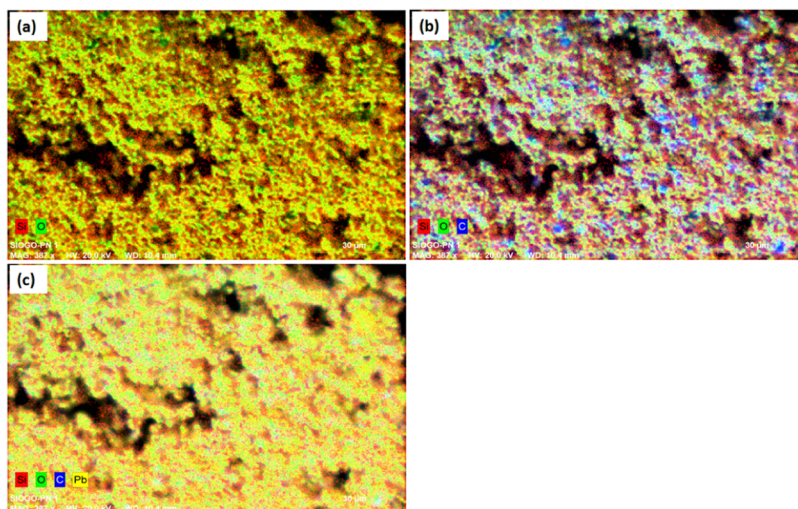
Figure 21. SEM-EDX mapping of (a) $MSiO_2$ NPs; (b) $MSiO_2$-GO nanosheets; and (c) lead uptake $MSiO_2$-GO nanosheets.
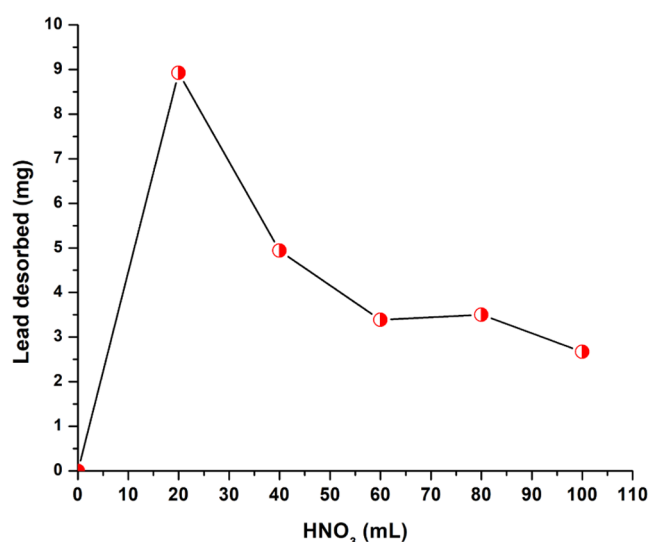
Figure 22. Regeneration of exhausted $MSiO_2$-GO nanosheets using 0.005 M HNO_3 as a desorbing agent.

adsorption of Pb^{2+} ions. The Langmuir isotherm models agreed well with sorption equilibrium data, which confirms the monolayer adsorption of Pb^{2+} on $MSiO_2$-GO nanosheets. The regeneration of the exhausted $MSiO_2$-GO nanosheets was successfully demonstrated. Thus, the synthesized $MSiO_2$-GO nanosheets can be considered simple, economical, biocompatible, and reusable adsorbents for the excellent removal of Pb^{2+} ions from water.

ASSOCIATED CONTENT

ⓢ Supporting Information

The Supporting Information is available free of charge at https://pubs.acs.org/doi/10.1021/acsomega.3c05228.

> BET surface area, pore volume and pore size distribution of the synthesized $MSiO_2$ NPs and $MSiO_2$-GO nanosheets obtained by measuring N_2 adsorption and desorption plot and comparative adsorption of Pb^{2+} ions onto $MSiO_2$-GO nanosheets with other reported nanosorbents (PDF)

AUTHOR INFORMATION

Corresponding Authors

Yana Bagbi − *Department of Physics and Astrophysics, University of Delhi, North Delhi 110007, India;* ⓞ orcid.org/0000-0001-6627-1661; Email: yanabagbi@gmail.com

Pratima R. Solanki − *Special Centre for Nanoscience, Jawaharlal Nehru University, New Delhi 110067, India;* ⓞ orcid.org/0000-0003-1679-2180; Email: pratimarsolanki@gmail.com

Complete contact information is available at:
https://pubs.acs.org/10.1021/acsomega.3c05228

Notes

The authors declare no competing financial interest.

REFERENCES

(1) Gao, W.; Majumder, M.; Alemany, L. B.; Narayanan, T. N.; Ibarra, M. A.; Pradhan, B. K.; Ajayan, P. M. Engineered graphite oxide materials for application in water purification. *ACS Appl. Mater. Interfaces* **2011**, *3* (6), 1821−1826.

(2) Madadrang, C. J.; Kim, H. Y.; Gao, G.; Wang, N.; Zhu, J.; Feng, H.; Gorring, M.; Kasner, M. L.; Hou, S. Adsorption behavior of EDTA-graphene oxide for Pb (II) removal. *ACS Appl. Mater. Interfaces* **2012**, *4* (3), 1186−1193.

(3) Nagajyoti, P. C.; Lee, K. D.; Sreekanth, T. Heavy metals, occurrence and toxicity for plants: a review. *Environ. Chem. Lett.* **2010**, *8*, 199−216.

(4) *Toxicological Profile for Lead US EPA. Air Quality Criteria for Lead* US Department of Health and Human Services, Agency for Toxic

Substances and Disease Registry (ATSDR), Public Health Service: Atlanta, GA; 2007.

(5) Järup, L. Hazards of heavy metal contamination. *Br. Med. Bull.* **2003**, *68* (1), 167−182.

(6) Bagbi, Y.; Sarswat, A.; Mohan, D.; Pandey, A.; Solanki, P. R. Lead and chromium adsorption from water using L-cysteine functionalized magnetite (Fe$_3$O$_4$) nanoparticles. *Sci. Rep.* **2017**, 7 (1), No. 7672.

(7) Bagbi, Y.; Sarswat, A.; Mohan, D.; Pandey, A.; Solanki, P. R. Lead (Pb^{2+}) adsorption by monodispersed magnetite nanoparticles: Surface analysis and effects of solution chemistry. *J. Environ. Chem. Eng.* **2016**, *4* (4), 4237−4247.

(8) Yang, H.; Xu, R.; Xue, X.; Li, F.; Li, G. Hybrid surfactant-templated mesoporous silica formed in ethanol and its application for heavy metal removal. *J. Hazard. Mater.* **2008**, *152* (2), 690−698.

(9) Sreeprasad, T. S.; Maliyekkal, S. M.; Lisha, K. P.; Pradeep, T. Reduced graphene oxide−metal/metal oxide composites: facile synthesis and application in water purification. *J. Hazard. Mater.* **2011**, *186* (1), 921−931.

(10) Geim, A. K. Graphene: status and prospects. *Science* **2009**, *324* (5934), 1530−1534.

(11) Yu, J.-G.; Yu, L.-Y.; Yang, H.; Liu, Q.; Chen, X.-H.; Jiang, X.-Y.; Chen, X.-Q.; Jiao, F.-P. Graphene nanosheets as novel adsorbents in adsorption, preconcentration and removal of gases, organic compounds and metal ions. *Sci. Total Environ.* **2015**, *502*, 70−79.

(12) Lü, K.; Zhao, G.; Wang, X. A brief review of graphene-based material synthesis and its application in environmental pollution management. *Chin. Sci. Bull.* **2012**, *57*, 1223−1234.

(13) Zhao, G.; Ren, X.; Gao, X.; Tan, X.; Li, J.; Chen, C.; Huang, Y.; Wang, X. Removal of Pb (II) ions from aqueous solutions on few-layered graphene oxide nanosheets. *Dalton Trans.* **2011**, *40* (41), 10945−10952.

(14) Ma, Y.; Di, H.; Yu, Z.; Liang, L.; Lv, L.; Pan, Y.; Zhang, Y.; Yin, D. Fabrication of silica-decorated graphene oxide nanohybrids and the properties of composite epoxy coatings research. *Appl. Surf. Sci.* **2016**, *360*, 936−945.

(15) Yang, K.; Chen, B.; Zhu, L. Graphene-coated materials using silica particles as a framework for highly efficient removal of aromatic pollutants in water. *Sci. Rep.* **2015**, *5* (1), No. 11641.

(16) Sardoiwala, M. N.; Kaundal, B.; Choudhury, S. R. Toxic impact of nanomaterials on microbes, plants and animals. *Environ. Chem. Lett.* **2018**, *16*, 147−160.

(17) Bhowmik, K.; Pramanik, S.; Medda, S. K.; De, G. Covalently functionalized reduced graphene oxide by organically modified silica: a facile synthesis of electrically conducting black coatings on glass. *J. Mater. Chem.* **2012**, *22* (47), 24690−24697.

(18) Bagbi, Y.; Pandey, A.; Solanki, P. R. Mesoporous Spherical Shaped Silica Nanoparticles for the Effective Adsorption of Aqueous Lead (Pb^{2+}). *Adv. Sci. Lett.* **2018**, *24* (2), 922−926.

(19) Dakshinamoorthy, P.; Vaithilingam, S. Platinum−copper doped poly (sulfonyldiphenol/cyclophosphazene/benzidine)−graphene oxide composite as an electrode material for single stack direct alcohol alkaline fuel cells. *RSC Adv.* **2017**, *7* (56), 34922−34932.

(20) Zhang, W.-H.; He, P.-P.; Wu, S.; Xu, J.; Li, Y.; Zhang, G.; Wei, X.-Y. Graphene oxide grafted hydroxyl-functionalized ionic liquid: A highly efficient catalyst for cycloaddition of CO$_2$ with epoxides. *Appl. Catal., A* **2016**, *509*, 111−117.

(21) Chaudhary, Y. S.; Ghatak, J.; Bhatta, U. M.; Khushalani, D. One-step method for the self-assembly of metal nanoparticles onto facetted hollow silica tubes. *J. Mater. Chem.* **2006**, *16* (36), 3619−3623.

(22) Nakamoto, K. *Infrared and Raman Spectra of Inorganic and Coordination Compounds, Part B: Applications in Coordination, Organometallic, and Bioinorganic Chemistry*; John Wiley & Sons, 2009.

(23) Abraham, S.; Ciobota, V.; Srivastava, S.; Srivastava, S. K.; Singh, R. K.; Dellith, J.; Malhotra, B.; Schmitt, M.; Popp, J.; Srivastava, A. Mesoporous silica particle embedded functional graphene oxide as an efficient platform for urea biosensing. *Anal. Methods* **2014**, *6* (17), 6711−6720.

(24) Kirk, C. T. Quantitative analysis of the effect of disorder-induced mode coupling on infrared absorption in silica. *Phys. Rev. B* **1988**, *38* (2), 1255.

(25) Zhong, L.; Yun, K. Graphene oxide-modified ZnO particles: synthesis, characterization, and antibacterial properties. *Int. J. Nanomed.* **2015**, *10*, 79−92, DOI: 10.2147/IJN.S88319.

(26) Hao, L.; Song, H.; Zhang, L.; Wan, X.; Tang, Y.; Lv, Y. SiO$_2$/graphene composite for highly selective adsorption of Pb (II) ion. *J. Colloid Interface Sci.* **2012**, *369* (1), 381−387.

(27) Huang, P.; Xu, C.; Lin, J.; Wang, C.; Wang, X.; Zhang, C.; Zhou, X.; Guo, S.; Cui, D. Folic acid-conjugated graphene oxide loaded with photosensitizers for targeting photodynamic therapy. *Theranostics* **2011**, *1*, 240.

(28) Xu, G.; Zhang, J.; Song, G. Effect of complexation on the zeta potential of silica powder. *Powder Technol.* **2003**, *134* (3), 218−222.

(29) Wang, Z. M.; Wang, W.; Coombs, N.; Soheilnia, N.; Ozin, G. A. Graphene oxide− periodic mesoporous silica sandwich nanocomposites with vertically oriented channels. *ACS Nano* **2010**, *4* (12), 7437−7450.

(30) Du, Y. C.; Huang, L. J.; Wang, Y. X.; Yang, K.; Zhang, Z. J.; Wang, Y.; Kipper, M. J.; Belfiore, L. A.; Tang, J. G. Preparation of graphene oxide/silica hybrid composite membranes and performance studies in water treatment. *J. Mater. Sci.* **2020**, *55*, 11188−11202.

(31) Peng, J.; Li, W.; Wu, Z.; Li, H.; Huang, Y.; Ouyang, Y.; Wang, Y.; Guo, X.; Chen, G.; Wang, X. Rational design and performance of ansode materials based on Si/SiO x/C particles anchored on graphene sheets. *ACS Appl. Energy Mater.* **2021**, *4* (5), 4966−4975.

(32) Rajput, S.; Pittman, C. U., Jr.; Mohan, D. Magnetic magnetite (Fe$_3$O$_4$) nanoparticle synthesis and applications for lead (Pb^{2+}) and chromium (Cr^{6+}) removal from water. *J. Colloid Interface Sci.* **2016**, *468*, 334−346.

(33) Chen, A.-H.; Liu, S.-C.; Chen, C.-Y.; Chen, C.-Y. Comparative adsorption of Cu (II), Zn (II), and Pb (II) ions in aqueous solution on the crosslinked chitosan with epichlorohydrin. *J. Hazard. Mater.* **2008**, *154* (1−3), 184−191.

(34) Chen, C.; Wang, X. Adsorption of Ni (II) from aqueous solution using oxidized multiwall carbon nanotubes. *Ind. Eng. Chem. Res.* **2006**, *45* (26), 9144−9149.

(35) Kumari, M.; Pittman, C. U., Jr.; Mohan, D. Heavy metals [chromium (VI) and lead (II)] removal from water using mesoporous magnetite (Fe3O4) nanospheres. *J. Colloid Interface Sci.* **2015**, *442*, 120−132.

(36) Liu, R.; Liang, P. Determination of trace lead in water samples by graphite furnace atomic absorption spectrometry after preconcentration with nanometer titanium dioxide immobilized on silica gel. *J. Hazard. Mater.* **2008**, *152* (1), 166−171.

(37) Cao, C.-Y.; Cui, Z.-M.; Chen, C.-Q.; Song, W.-G.; Cai, W. Ceria hollow nanospheres produced by a template-free microwave-assisted hydrothermal method for heavy metal ion removal and catalysis. *J. Phys. Chem. C* **2010**, *114* (21), 9865−9870.

(38) Mahdavi, M.; Ahmad, M. B.; Haron, M. J.; Gharayebi, Y.; Shameli, K.; Nadi, B. Fabrication and characterization of SiO 2/(3-aminopropyl) triethoxysilane-coated magnetite nanoparticles for lead (II) removal from aqueous solution. *J. Inorg. Organomet. Polym. Mater.* **2013**, *23*, 599−607.

(39) Ma, X.; Wang, Y.; Gao, M.; Xu, H.; Li, G. A novel strategy to prepare ZnO/PbS heterostructured functional nanocomposite utilizing the surface adsorption property of ZnO nanosheets. *Catal. Today* **2010**, *158* (3−4), 459−463.

(40) Zhong, L. S.; Hu, J. S.; Liang, H. P.; Cao, A. M.; Song, W. G.; Wan, L. J. Self-Assembled 3D flowerlike iron oxide nanostructures and their application in water treatment. *Adv. Mater.* **2006**, *18* (18), 2426−2431.

(41) Huang, S.-H.; Chen, D.-H. Rapid removal of heavy metal cations and anions from aqueous solutions by an amino-functionalized magnetic nano-adsorbent. *J. Hazard. Mater.* **2009**, *163* (1), 174−179.